Atmos. Meas. Tech. Discuss., 8, 11029–11075, 2015
www.atmos-meas-tech-discuss.net/8/11029/2015/
doi:10.5194/amtd-8-11029-2015

Atmospheric Measurement Techniques Discussions

Retrieval of near-surface sulfur dioxide (SO_2) concentrations at a global scale using IASI satellite observations

S. Bauduin[1], L. Clarisse[1], J. Hadji-Lazaro[2], N. Theys[3], C. Clerbaux[1,2], and P.-F. Coheur[1]

[1]Spectroscopie de l'Atmosphère, Service de Chimie Quantique et Photophysique, Université Libre de Bruxelles (ULB), Brussels, Belgium
[2]Sorbonne Universités, UPMC Univ. Paris 06, Université Versailles St-Quentin, CNRS/INSU, LATMOS-IPSL, Paris, France
[3]Belgian Institute for Space Aeronomy (BIRA-IASB), Brussels, Belgium

Received: 25 August 2015 – Accepted: 30 September 2015 – Published: 26 October 2015

Correspondence to: S. Bauduin (sbauduin@ulb.ac.be)

Published by Copernicus Publications on behalf of the European Geosciences Union.

Abstract

SO_2 from volcanic eruptions is now operationally monitored from space in both ultraviolet (UV) and thermal infrared (TIR) spectral range, but anthropogenic SO_2 has almost solely been measured from UV sounders. Indeed, TIR instruments are well-known to have a poor sensitivity to the boundary layer (PBL), due to generally low thermal contrast (TC) between the ground and the air above it. Recent studies have demonstrated the capability of the Infrared Atmospheric Sounding Interferometer (IASI) to measure near-surface SO_2 locally, for specific atmospheric conditions. In this work, we develop a retrieval method allowing the inference of SO_2 near-surface concentrations from IASI measurements at a global scale. This method consists of two steps. Both are based on the computation of radiance indexes representing the strength of the SO_2 ν_3 band in IASI spectra. The first step allows retrieving the peak altitude of SO_2 and selecting near-surface SO_2. In the second step, 0–4 km columns of SO_2 are inferred using a look-up table (LUT) approach. Using this new retrieval method, we obtain the first global distribution of near-surface SO_2 from IASI-A, and identify the dominant anthropogenic hotspot sources and volcanic degassing. The 7-year daily time evolution of SO_2 columns above two industrial source areas (Beijing in China and Sar Cheshmeh in Iran) is investigated and correlated to the seasonal variations of the parameters that drive the IASI sensitivity to the PBL composition. Apart from TC, we show that humidity is the most important parameter which determines IR sensitivity to near-surface SO_2. As IASI provides twice daily global measurements, the differences between the retrieved columns for the morning and evening orbits are investigated. This paper finally presents a first intercomparison of the measured 0–4 km columns with an independent iterative retrieval method and with observations of the Ozone Monitoring Instrument (OMI).

AMTD
8, 11029–11075, 2015

1 Introduction

Sulfur dioxide (SO_2) is an atmospheric trace gas with both natural and anthropogenic sources. Volcanic emissions are the largest natural contributors to tropospheric and stratospheric SO_2, and account for 7.5–10.5 Tg of S per year on average (Andres and Kasgnoc, 1998; Halmer et al., 2002). Anthropogenic sources emit on average 60–100 Tg of S per year (Stevenson et al., 2003), with the major contribution coming from combustion of sulfur-rich fuels, such as coal and oil, and smelting of heavy metals (Smith et al., 2011). The sinks of SO_2 are dry (Wesely, 2007) and wet (Ali-Khodja and Kebabi, 1998) deposition, and oxidation by the OH radical in the gas phase or by O_3 and H_2O_2 in the aqueous phase (Eisinger and Burrows, 1998; Stevenson et al., 2003). The SO_2 lifetime varies according to the sinks from a few hours to several days (Lee et al., 2011).

SO_2 emissions of most volcanoes are now well monitored from space, especially eruptive degassing. Significant amounts of SO_2 are in this case mainly injected in the high troposphere or stratosphere and cover large areas. In the ultraviolet (UV), retrievals of volcanic SO_2 have started in 1978 with the TOMS (Total Ozone Mapping Spectrometer) instrument (Krueger, 1983; Carn et al., 2003) and have continued since then with GOME (Global Ozone Monitoring Experiment) (Eisinger and Burrows, 1998), SCIAMACHY (SCanning Imaging Absorption spectroMeter for Atmospheric CHartography) (Lee et al., 2008), GOME-2 (Rix et al., 2009) and OMI (Ozone Monitoring Instrument) (Krotkov et al., 2006). In the thermal infrared (TIR), volcanic SO_2 has been measured from multi-channel instruments with moderate resolution (e.g. Realmuto and Watson, 2001; Watson et al., 2004) and later with high-spectral resolution instruments such as TES (Tropospheric Emission Spectrometer) (Clerbaux et al., 2008), AIRS (Atmospheric Infrared Sounder) (Carn et al., 2005) and IASI (Infrared Atmospheric Sounding Interferometer) (Clarisse et al., 2008).

In contrast to volcanoes, SO_2 pollution from anthropogenic activities is difficult to monitor because it is often confined horizontally and vertically. In the UV, different meth-

AMTD
8, 11029–11075, 2015

ods have successfully been developed to retrieve surface SO_2. These are included in different global products such as the operational planetary boundary layer (PBL) OMI SO_2 product (Krotkov et al., 2006, 2008) or the recent OMI algorithm based on a multi-windows DOAS (Differential Optical Absorption Spectroscopy) scheme developed by Theys et al. (2015). The latter will be used for comparison purposes later in this paper. The availability of the satellite-derived columns from the UV nadir sounders have allowed inferring SO_2 anthropogenic emissions (e.g. Carn et al., 2007; Fioletov et al., 2011, 2013, 2015; McLinden et al., 2012, 2014). This has not yet been possible from TIR instruments, which suffer from lower sensitivity to the near-surface atmosphere due to generally low temperature differences between the surface and the PBL atmosphere (hereafter called thermal contrast). Recently Bauduin et al. (2014) and Boynard et al. (2014) have nevertheless demonstrated the capability of IASI to measure near-surface SO_2 locally. Both studies revealed that the presence of large thermal inversions (associated to high negative thermal contrasts) and low humidity (preventing opacity in the ν_3 band) have allowed retrieving near-surface SO_2. However, the detection of SO_2 by IASI could theoretically be achieved in other situations, particularly in case of large positive thermal contrasts, which correspond to a surface much hotter than the atmosphere. This is demonstrated and discussed in Sect. 3, which provides the first global distributions of near-surface SO_2 from IASI over the period 2008–2014. The method used to retrieve SO_2 columns, described thoroughly in Sect. 2, relies on the calculation of a hyperspectral radiance index (HRI), similarly to the work of Van Damme et al. (2014) for ammonia (NH_3). As the aim of this work consists of retrieving near-surface SO_2, the determination of the altitude of SO_2 defines the first step of the method and relies on the work of Clarisse et al. (2014). It is used to remove all plumes located above 4 km of height, which likely correspond to volcanic eruptions. The retrieval of 0–4 km SO_2 columns is performed in a second step, where calculated HRI are converted into columns using a look-up tables (LUT) approach. This calculation is performed using only the ν_3 band spectral region (1300–1410 cm^{-1}). The use of the ν_1 spectral

AMTD
8, 11029–11075, 2015

band (around 1100–1200 cm^{-1}) is not considered in this work. The whole procedure is described in Sect. 2.

2 SO_2 near-surface product

2.1 IASI and methodology

The IASI instrument is a Michelson interferometer onboard MetOp platforms (A and B) circling the Earth on a Sun synchronous polar orbit. The IASI effective field of view is composed of 2 × 2 footprints of 12 km diameter each at nadir. IASI has a global coverage twice a day thanks to a swath of 2200 km and two overpasses per day (morning at 09:30 and evening at 21:30 LT at the equator). The instrument covers the thermal infrared spectral range from 645 to 2760 cm^{-1} with a spectral resolution of 0.5 cm^{-1} after apodization. Each measurement consists of 8461 radiance channels (0.25 cm^{-1} sampling) and is characterized by a noise of 0.2 K on average. Details about the instrument can be found elsewhere (Clerbaux et al., 2009; Hilton et al., 2012). Only measurements of the IASI-A instrument have been considered here.

The methodology used in this work to retrieve near-surface SO_2 amount relies on the sensitive detection method of trace gases introduced by Walker et al. (2011), and used later by Van Damme et al. (2014) for retrieving NH_3 columns at global scale from IASI. Retrieval approaches based on spectral fitting generally consist of simultaneous iterative adjustments of the atmospheric parameters of interest (here the 0–4 km SO_2 column) and spectrally interfering unknown variables. The idea of the proposed method is to consider the interfering variables as permanent unknowns and to incorporate them in a generalized noise covariance matrix **S**. This matrix should include all variability coming from the parameters affecting the IASI spectrum in the spectral range under consideration (here 1300–1410 cm^{-1} corresponding to the ν_3 band) but not SO_2. In this way, instead of iteratively adjusting the SO_2 columns and the interfering parameters,

AMTD
8, 11029–11075, 2015

a normalized radiance index is calculated according to:

$$\mathrm{HRI} = \frac{\boldsymbol{K}^T \mathbf{S}^{-1}(\boldsymbol{y} - \overline{\boldsymbol{y}})}{\sqrt{\boldsymbol{K}^T \mathbf{S}^{-1} \boldsymbol{K}}}, \quad (1)$$

where $\boldsymbol{K}$ is a Jacobian, a derivative of the IASI spectrum $\boldsymbol{y}$ with respect to SO_2, $\overline{\boldsymbol{y}}$ is the mean background spectrum with no detectable SO_2 associated with the matrix **S**. This matrix **S** acts as a weight in the projection of the observed spectrum onto SO_2 signature, giving more importance to IASI channels less influenced by interfering parameters. Practically, $\overline{\boldsymbol{y}}$ and **S** are built from a sufficiently large sample of SO_2-free IASI spectra to include the global atmospheric variability in the absence of SO_2 (see Sects. 2.2 and 2.3).

The HRI, which is unitless, can be seen as an index of detection, whose value represents the strength of the SO_2 signal in the IASI radiance spectrum, which is related to the amount of SO_2 in the atmosphere. The larger its value, the more likely is the enhancement of the gas. An ensemble of SO_2-free spectra has a mean HRI of 0 and a standard deviation of 1, and a HRI of 3 (which corresponds to 3σ) can reasonably be considered as the limit of detection. Because the HRI does not correspond to the real column of SO_2, it is therefore needed to convert it in a subsequent step. This can be done by using look-up tables built from forward model simulations, which link the simulated HRI values to known SO_2 columns. Prior to this, as this work focuses on near-surface pollution, we use the algorithm of Clarisse et al. (2014) to select the spectra with detectable low altitude SO_2 enhancements. Only plumes located below 4 km are kept. These successive steps of the retrieval scheme are detailed in next sections.

AMTD
8, 11029–11075, 2015

2.2 Retrieval of the altitude of the plume

The altitude of SO_2 is retrieved using the algorithm presented in Clarisse et al. (2014). In short, a HRI is computed for different altitudes following:

$$\mathrm{HRI}(h) = \frac{\boldsymbol{K}_h^T \mathbf{S}^{-1} (\boldsymbol{y} - \overline{\boldsymbol{y}})}{\sqrt{\boldsymbol{K}_h^T \mathbf{S}^{-1} \boldsymbol{K}_h}}, \quad (2)$$

where the $\boldsymbol{K}_h$ is the Jacobian for SO_2 located at an altitude h. If there is a detectable amount of SO_2, the function HRI(h) will peak at the altitude of the plume. Indeed, the overlap between the IASI spectrum and the SO_2 spectral signature is maximal at this altitude. The height determination therefore consists in calculating the function HRI(h) and finding the altitude of its maximum.

To this end, Jacobians $\boldsymbol{K}_h$ have been pre-calculated with the finite difference method for the spectral range 1300–1410 cm^{-1} using monthly averaged H_2O and temperature profiles in $10^\circ \times 20^\circ$ boxes. These averages were calculated from the meteorological fields from the EUMETSAT L2 Product Processing Facility (PPF) (Schlüssel et al., 2005; August et al., 2012) using the 15 of each month of 2009, 2011 and 2013. One set of 30 vectors $\boldsymbol{K}_h$ has been generated for each box and for each month, considering 1 km thick layer of 5 DU (1 Dobson Unit = 2.69×10^{16} molecules cm^{-2}) of SO_2, located every 1 km from 1 to 30 km. For each IASI observation, local Jacobians are then calculated using a bilinear interpolation of the four closest grid boxes, to better take into account the variation of the atmospheric conditions when observations move away from the center of the boxes. The mean background spectrum $\overline{\boldsymbol{y}}$ and the associated covariance matrix $\mathbf{S}$ needed to calculate the HRI (Eq. 2) have been built using a sample of one million randomly chosen IASI spectra. Those with detectable SO_2 have been filtered out using an iterative approach: first, spectra with observable SO_2 signatures were rejected using a brightness temperature difference method (see Clarisse et al., 2008, for details) and a first estimate of the matrix $\mathbf{S}$ is made. The second step uses

AMTD
8, 11029–11075, 2015

this initial matrix to exclude spectra with measurable HRI from the remaining set of measurements (a similar method is used in Van Damme et al., 2014; Clarisse et al., 2013). Similarly to the Jacobians, $\overline{\boldsymbol{y}}$ and **S** are calculated over the spectral range 1300–1410 cm^{-1}.

As explained in Clarisse et al. (2014), because of the use of averaged Jacobians, the retrieved altitude can be biased, especially close to the surface. The best accuracy is achieved between 5 and 15 km, and the altitude estimate is provided within 1–2 km. Below 5 km, the retrieved altitude is more uncertain. However, this is not an important issue here as the altitude is used only to filter out SO_2 plumes emitted by volcanoes directly in the free troposphere. In the following, only plumes located between the surface and 4 km above ground are selected. The retrieved SO_2 corresponds therefore to a 4 km thick layer (hereafter called 0–4 km column).

2.3 Retrieval of near-surface SO_2 concentrations – Look-up tables

For the low SO_2 plumes, the next step consists in computing an HRI (according to Eq. 1) for each IASI measurement and converting it to a SO_2 column. Different Jacobian, $\overline{\boldsymbol{y}}$ and **S** have been built for this second step (see section below). Because a constant Jacobian is used in the calculation of the HRI, there are several parameters that impact its value in addition to the SO_2 abundance itself and they need to be accounted for. We have considered the impact of viewing angle (by building angle-dependent matrices for the HRI calculation; see Sect. 2.3.1) and the one of humidity and thermal contrast, which are separate entries in the look-up-tables (Sect. 2.3.2).

2.3.1 Angular dependency

The dependence of the signal strength on the viewing angle has to be taken account in the conversion of HRI values. As reported by Van Damme et al. (2014), the application of a cosine factor to account for the increased path length tends to overcorrect the HRI and leads to a bias for larger angles. As they suggested, angular dependent $\boldsymbol{K}$, $\overline{\boldsymbol{y}}$, **S**

AMTD
8, 11029–11075, 2015

have been used. Specifically, between 0° and 55°, 5° angle bins have been defined and a last one of 4° is considered for 55–59° (IASI zenith angle ranges between 0° and 58.8°). For the median angle of each bin, a Jacobian has been generated for a standard atmosphere (Anderson et al., 1986), with a scaling factor applied to the methane profile according to Bauduin et al. (2014). A thermal contrast of 10 K has been considered. All $\boldsymbol{K}$ have been calculated with the finite difference method for 200 ppb SO_2 well-mixed between 4 and 5 km, and over the 1300–1410 cm^{-1} range. For $\overline{\boldsymbol{y}}$ and $\mathbf{S}$ almost the totality of cloud-free (i.e. cloud fraction below 20 % and available Eumetsat L2 surface temperature, atmospheric temperature and H_2O profiles) observations of the 15 of each month of 2009 and 2011 have been used, sorted by angle bins. Measurements with detectable SO_2 have been filtered as above. In this way, for each angle bin, $\overline{\boldsymbol{y}}$ and $\mathbf{S}$ have been calculated from about 750 000 spectra.

2.3.2 Look-up tables

The conversion of the HRI into SO_2 column is done using look-up tables, which, as for $\overline{\boldsymbol{y}}$ and $\mathbf{S}$, have been separated per angle bin. The LUTs include 4 dimensions linking thermal contrast, total column of water, HRI and SO_2 column. To build the LUT, forward simulations of IASI spectra have been performed for a series of situations, summarized in Table 1, using the line-by-line Atmosphit software (Coheur et al., 2005). More specifically the following parameters were varied to provide a representative set of atmospheric conditions:

SO_2 columns: To obtain a reference SO_2 vertical profile for anthropogenic emissions, we relied on global chemistry transport MOZART model (Emmons et al., 2010) outputs of January, April, July and October 2009 and 2010. An average profile was calculated from all modeled profiles above Eastern United States, Europe and Eastern China, with the SO_2 concentration above 4 km set to zero. The resulting reference profile is shown in Fig. 1 (blue). The set of atmospheric SO_2 columns included in the LUT was then obtained by scaling this reference profile by the 16 factors listed in Table 1, leading to a range of 0–4 km SO_2 columns (ground to 4 km above it) going from 0 to 415 DU.

AMTD
8, 11029–11075, 2015

H_2O: In a similar way, the water vapor profile from the US Standard model (Fig. 1 in red) has also been varied using 16 scaling factors (Table 1), covering a range of H_2O total column from 9.5×10^{19} to 2.3×10^{23} molecules cm^{-2}.

Temperature: A single temperature profile has been used (US standard, Fig. 1 right). To include a range of thermal contrast values, which are defined as the difference between the temperature of the ground and the temperature of the air at 500 m (see Fig. 1), we have varied the surface temperature to provide 25 different situations, listed in Table 1. These include extreme cases of thermal contrasts, from −30 to +40 K, but also a range of low and moderate values. Note that a thermal contrast of 0 corresponds to an isothermal 0–1 km layer and implies that the outgoing radiance of this layer is that of a blackbody (Bauduin et al., 2014). Note also that a constant emissivity of 0.98 has been used in the forward simulations. The emissivity can indeed be shown to be almost constant over the spectral range considered, but also temporally and spatially (Zhou et al., 2013).

The LUTs constructed as described above have been interpolated on a finer grid (TC, H_2O and SO_2 dimensions). An example of resulting LUT is shown in Fig. 2a (for constant water vapor) and 2b (for constant thermal contrast). The retrieval scheme consists in determining for each IASI measurement the satellite zenith angle, the HRI, the thermal contrast, the total column of water vapor and, using the LUT, the 0–4 km column of SO_2.

From Fig. 2, it can be seen that the HRI has the same sign as thermal contrast. In case of positive thermal contrast, this is explained by the fact that SO_2 spectral lines are in absorption in IASI measurements, resulting in a negative difference $(\boldsymbol{y} - \overline{\boldsymbol{y}})$. Given the fact that the Jacobians are also negative (see definition in Sect. 2.3.1), the calculated HRI is positive. As a rule, for constant zenith angle, column of H_2O and SO_2, the value of the HRI increases with the thermal contrast. This increase in spectral signal corresponds to an increase of IASI sensitivity to near-surface SO_2. However (see Fig. 2b for a constant TC of 15 K), for increasing water vapor, which renders the atmosphere opaque in the low layers, the IASI sensitivity decreases along with the

AMTD
8, 11029–11075, 2015

HRI for constant SO_2 columns, thermal contrast and viewing angle. In case of negative thermal contrast, SO_2 lines are in emission and the calculated HRI is negative too. For decreasing negative thermal contrast, the HRI value usually decreases. But from Fig. 2a it can be seen that some HRI values are positive for negative thermal contrasts. We explored this seemingly odd behavior with the help of Fig. 3 (left), which shows HRI as a function of SO_2 for a thermal contrast of −10 K and a total column of H_2O of 2.4×10^{20} molecules cm^{-2}. From 0 to 66.33 DU, HRI decreases for increasing SO_2. Above 66.33 DU, the HRI starts to increase with increasing SO_2. From about 250 DU, the HRI becomes positive. This behavior can be explained by the competition between emission (mainly in the 0–1 km layer) and absorption (above 1 km). Figure 3 (right) presents the contributions (in absolute value) of the emission in the 0–1 km layer and the absorption in the 1–4 km layer to the total spectral signal as function of the 0–4 km SO_2 column. They have been evaluated at 1355 cm^{-1} using similar techniques as in Clarisse et al. (2010). In Fig. 3, for columns ranging from 0 to 66.33 DU, emission in the 0–1 km layer increases more rapidly than absorption in the 1–4 km layer. This results in decreasing HRI (more and more negative). From 66.33 DU, emission comes closer to saturation; its increase is slower than the one of absorption, whose saturation occurs for larger SO_2 columns, and the HRI begins to increase. From around 250 DU, absorption totally counterbalances emission and HRI values become positive. This competition between emission in the lowest layers and absorption higher up depends on the value of the temperature inversion, as the latter determines the strength of the emission. Note that this competition also depends on the altitude of the thermal inversion, but which is here constant (just above the ground). The consequence is that, for negative thermal contrast, a negative HRI can be converted into two SO_2 columns (see Fig. 3, left): a small one (emission combined with lower absorption above 1 km) and a large one (larger emission partly counterbalanced by a more rapid increase of absorption above 1 km). In that case, because the very large columns included in the LUTs are not expected above anthropogenic sources, only the smallest one is considered. Note

AMTD
8, 11029–11075, 2015

that the large columns for which the HRI is positive for negative thermal contrast have been kept.

From the LUT, we can estimate the detection limit of IASI to near-surface SO_2. In Fig. 4, the lowest detectable 0–4 km column of SO_2 is presented as function of thermal contrast and the total column of H_2O. These columns have been calculated using the LUT assuming a detection threshold of 3 on the value of HRI (see Sect. 2.1). As expected, this limit of detection largely depends on thermal contrast and humidity. Indeed, when the former is close to 0, IASI stays insensitive even to large SO_2 columns. For large thermal contrasts, 0–4 km columns lower than 1 DU can be measured. This also depends on the humidity. Below 2×10^{22} molecules cm^{-2}, the limit of detection stays below 2 DU for both high positive and high negative thermal contrasts. For larger H_2O amount, this limit rapidly increases for negative thermal contrast but stays relatively low for large positive thermal contrasts. From above 4×10^{22} molecules cm^{-2} of H_2O, the detection threshold starts to increase for positive thermal contrasts.

2.3.3 Error characterization

To each LUT, an associated table of errors has been generated by propagating the uncertainties of the different LUT parameters:

$$\sigma_{SO_2} = \sqrt{\left(\frac{\partial SO_2}{\partial TC}\right)^2 \sigma_{TC}^2 + \left(\frac{\partial SO_2}{\partial H_2O}\right)^2 \sigma_{H_2O}^2 + \left(\frac{\partial SO_2}{\partial HRI}\right)^2 \sigma_{HRI}^2}, \quad (3)$$

where σ_{SO_2} is the absolute error of the SO_2 column, σ_{TC} and σ_{H_2O} are the errors on thermal contrast and total column of water vapor, which are respectively taken equal to $\sqrt{2}$ K and 10 % relying on early validation of the IASI level 2 meteorological fields from the PPF (Pougatchev et al., 2009); σ_{HRI} is the standard deviation of the HRI and is equal to 1.

An example of an error table is given in Fig. 5 for the angle bin 0–5° and for a total column of water vapor of 2×10^{20} molecules cm^{-2}. As expected, the errors are directly

AMTD
8, 11029–11075, 2015

linked to the IASI sensitivity to near-surface SO_2, with large errors (above 100 %) occurring in case of small thermal contrasts. The errors decrease with increasing thermal contrasts and drop to 20 % or less in the most favorable situations. As discussed above, for large total columns of H_2O, IASI is also less sensitive to near-surface SO_2 and errors increase accordingly. The errors are used in the following to filter out the data in the distributions and time series and only the retrieved columns for which the conditions of surface sensitivity are fulfilled are used.

3 Results

3.1 Global distributions

The SO_2 retrievals have been performed on 7 years of IASI observations (1 January 2008–30 September 2014). In Fig. 6, an average global distribution of the near-surface column of SO_2 for this period is presented, separately for day (top) and night (bottom) observations. Only measurements with less than 20 % cloud fraction in the IASI field-of-view and with available surface temperature, profiles of temperature and H_2O from the EUMETSAT IASI level 2 PPF have been used. Furthermore, only retrieved SO_2 columns with less than 25 % relative error and less than 10 DU absolute error are used. The second criterion was necessary to remove spurious data over the cold Antarctic region. The columns that pass these posterior filters have been averaged on a $0.5^\circ \times 0.5^\circ$ grid for cells including more than 5 IASI measurements. The bottom-right inset in the daytime map presents the global anthropogenic emissions (in $kg\,s^{-1}\,m^{-2}$) of SO_2 provided by the EDGAR v4.2 inventory (downloaded from the ETHER/ECCAD database) (EDGAR-Emission Database for Global Atmos. Res., 2011).

Figure 6 reveals several anthropogenic and volcanic hotspots, numbered from 1 to 13. Most of them are observed during the morning overpass, when the thermal contrast is large. They are:

AMTD
8, 11029–11075, 2015

1. *China*: China is one of the world's largest emission sources of SO_2, mainly due to energy supply through coal combustion (Lu et al., 2010; Smith et al., 2011; Lin et al., 2012). A large region of enhanced SO_2 columns, from 1 to 8 DU on the 7 year average, is seen over the industrial area surrounding Beijing. The largest columns are found close to Beijing, where emissions are the largest according to EDGAR database, and then decrease westwards.

2. *Norilsk*: Located above the Polar Circle, Norilsk is an industrial area where heavy metals are extracted from sulfide ores. It is also well-known for its extremely high levels of pollution (Blacksmith Institutes, 2007), and more particularly for its emissions of SO_2 (AMAP, 1998, 2006). The Norilsk smelters are also observed with IASI in Fig. 6, with averaged SO_2 columns varying between 1 and 9 DU. A comparison between measurements obtained in this work and those retrieved using an optimal estimation method (Bauduin et al., 2014) is given in Sect. 3.4.1.

3. *South Africa*: In Fig. 6, large SO_2 columns are observed close to Johannesburg in South Africa, with averaged columns around 3 DU for daytime measurements. Emissions of about 5×10^{-11} kg s^{-1} m^{-2} are reported in the EDGAR database in this area, which correspond to power plants of the Mpumalanga Highveld industrial region (Josipovic et al., 2009).

4. *Iran*: Several SO_2 sources are observed above Iran. Columns of 1 to 4 DU are measured above the smelters of Sar Cheshmeh copper complex (Rastmanesh et al., 2010, 2011). Emissions of oil industries located on the Khark Island (Ardestani and Shafie-Pour, 2009; Fioletov et al., 2013) are also observed, with columns around 1 to 2 DU.

5. *Balkhash*: In Fig. 6, we can see that IASI is able to measure SO_2 above the region of copper smelters located in Balkhash, Kazakhstan (Nadirov et al., 2013; Fioletov et al., 2013). Columns around 1 to 2 DU are retrieved.

AMTD
8, 11029–11075, 2015

6. *Mexico and Popocatepetl*: Columns reaching more than 10 DU are measured in the region of Mexico City and are regularly detected. These can be attributed to low altitude plume released by the Popocatepetl volcano (Varley and Taran, 2003; Grutter et al., 2008) and/or to SO_2 emissions of the Tula industrial complex, located northward to Mexico City (De Foy et al., 2009). The proximity of these two sources does not however allow separating their individual contribution by using only IASI observations.

7. *Kamchatka volcanoes*: SO_2 columns of about 2–3 DU are observed above the Kamchatka region. These probably correspond to the activity of different volcanoes located in this region (e.g. Kearney et al. (2008); see also the archive of the Global Volcanism Program: http://volcano.si.edu/).

8. *Nyiragongo*: Above the Democratic republic of the Congo, a plume with columns larger than 10 DU is detected. It corresponds to SO_2 volcanic degassing from Nyiragongo (Carn et al., 2013) and also probably to emissions of its neighbor, the Nyamuragira (Campion, 2014).

9. *Etna*: In Fig. 6, the Mount Etna is covered by SO_2, with 0–4 km columns around 6 DU. This volcano is known for its periodic degassing activity and lava fountaining events (Tamburello et al., 2013; Ganci et al., 2012).

10. *Andes*: A large SO_2 plume, with columns around 2–3 DU, is observed in the region of the Andes and can have several origins, which are difficult to distinguish. In the South of Peru, some volcanoes showed activity in the last years (e.g. Ubinas or Sabancaya, see the archive of the Global Volcanism Program: http://volcano.si.edu/). Copper smelters are located in Ilo (Carn et al., 2007), close to the coast, but are southern of the observed plume. SO_2 measured above Bolivia and Chile can originate from active volcanoes of the central Andean volcanic zone (Tassi et al., 2011, e.g. the Putana volcano, Stebel et al., 2015). Smelters are also located in this area (Huneeus et al., 2006) and anthropogenic emissions are reported

AMTD
8, 11029–11075, 2015

by the EDGAR database. The presence of an artefact in this region, due to the difficulty to represent the emissivity, can however not be totally rejected. Finally, SO_2 measured above Argentina, Ecuador and Colombia is mainly emitted by local volcanoes (Global volcanism Program, http://volcano.si.edu/).

11. *Bulgaria*: A narrow plume, with SO_2 columns of about 2 DU, is observed in Bulgaria. This corresponds to the Maritsa-Iztok complex of thermal power plants located close to Galabovo and Radnevo (Eisinger and Burrows, 1998; Prodanova et al., 2008).

12. *Turkey*: In Turkey, lignite-fired power plants are located in different regions and are known to cause air pollution in the vicinity of the complexes (Say, 2006; Vardar and Yumurtaci, 2010). The emissions of these are observed by IASI, with SO_2 columns around 2–3 DU.

One unexpected pattern in the daytime distribution is the SO_2 plume at the extreme Western part of China, corresponding to the Taklamakan desert (number 13). In this region, the EDGAR inventory only documents a few of small sources but no strong ones are known. While this could be explained by an artefact of the calculated HRI due to sand emissivity, which strongly affects the thermal infrared measurements, it is noteworthy that the issue is not observed similarly above other deserts. For instance, in Fig. 7 we compare the distribution of measured HRI and the total column of H_2O for three desert regions: the Sahara, the center of Australia and the Taklamakan. We observe that the HRI values are for almost 90 % of the cases below the detection limit of 3 above the Sahara and Australian deserts, whereas 30 % of the measurements over the Taklamakan are associated to a HRI between 3 and 5, in a few cases even above. It is therefore likely that the measured columns are real, with SO_2 being transported from the source regions in East China over the desert or being emitted there by developing gas and oil industries (Lin et al., 2013, http://www.cnpc.com.cn/en/Taklamakan/Taklamakan.shtml). The very high thermal contrast (up to 20 K) and very low humidity conditions found jointly in that region

AMTD
8, 11029–11075, 2015

make it indeed possible to measure such weak columns. Finally, the low-altitude parts of the plume released by the Nabro eruption, which followed complex transport patterns (Clarisse et al., 2014), are also seen during day above Ethiopia. Note that SO_2 is observed above Iceland and corresponds to the Bardarbunga eruption that started in September 2014 (Schmidt et al., 2015). The different conditions and filters applied on IASI measurements (see the beginning of this section) are responsible for the smallness of the area covered by SO_2.

It is worth emphasizing that some of the measured points in the 7 year average are only representative of one year. For continuous/permanent sources, this indeed depends on the inter-annual variation of thermal contrast and water vapor that limit IASI sensitivity. Moreover, some particular events are typical of some years, like volcanic eruptions.

Comparison with the EDGAR database has allowed identifying observed SO_2 plumes. It also points out the sources missed by IASI. Almost yearly low thermal contrasts (January–March and September–December) combined with high humidity in summer (May to September) are probably responsible for the absence of Eastern United-States and Eastern Europe sources in Fig. 6. Sources in India and in South Eastern Asia are also not observed by IASI, likely because of large H_2O amount in the atmosphere in the tropical region. The problem of these missing sources is not limited to IASI. Indeed, OMI global distributions reveal the absence of some of them: South Eastern Asia, part of Europe and part of India (Theys et al., 2015). These absences are possibly caused by unfavorable geophysical conditions (presence of clouds, ...), but this has to be investigated deeper. However, qualitatively, OMI and IASI global distributions are in good agreement. Both instruments are able to measure large sources such as Northeast China as well as small ones, like power plants in Turkey or Bulgaria. The two sounders are also complementary: regions characterized by high humidity and/or low thermal contrasts can be measured by OMI whereas IASI better monitors SO_2 at high latitudes, especially during the winter, and is not limited to daytime.

AMTD
8, 11029–11075, 2015

When examining Fig. 6 the differences between the SO_2 distributions retrieved from IASI measurements during morning (top) and evening (bottom) overpasses are also striking. In the evening distribution the plumes are more confined spatially and the columns at the center of the plumes generally larger by about a factor 3. These differences will be discussed in more details in Sect. 3.3. after the description of the time series below, which brings additional clues on this difference.

3.2 Time series

In Fig. 8, the 7 year time series (1 January 2008–30 September 2014) above Beijing and the smelters region of Sar Cheshmeh (Iran) are presented as examples. For both areas, daily averages of near-surface SO_2 columns, thermal contrast and H_2O total column are shown, separately for the morning (blue) and evening (red) overpasses of IASI. The averages have been calculated in a circle of 125 and 75 km radius around respectively Beijing and Sar Cheshmeh. As before, only observations with less than 20 % cloud fraction and with available meteorological level 2 have been taken into account and only those with sufficiently low retrieval errors are considered (same thresholds as before).

For Beijing and Sar Cheshmeh, the daily-averaged SO_2 columns from the morning overpass vary around 3 DU, with maxima that can reach 15 DU and 25 DU respectively. The time series is incomplete for Beijing, with successful SO_2 retrievals from December to May associated with fairly high thermal contrast (10 K on average but up to 20 K; Fig. 8 middle) and low humidity (below 5×10^{22} molecules cm^{-2}; Fig. 8 bottom). The favorable thermal contrast conditions persist mostly year-round in Beijing but the humidity is too high during the other months to allow IASI probing the surface. For Sar Cheshmeh, the time series of SO_2 columns from the IASI morning overpass is more extensive and this is due to the dryness of the site as compared to Beijing (a factor 2), combined with also persisting high thermal contrast conditions, from 10 K in the colder months to more than 30 K in summer.

AMTD
8, 11029–11075, 2015

It is clearly seen in Fig. 8 that IASI is mostly not sensitive to surface SO_2 above the two sites in the evening due to the drop of thermal contrast close to 0. As already noted in the previous section, the retrieved SO_2 columns are larger by at least a factor 3 in the evening compared to the morning (red vs. blue symbols). This is further investigated in next section.

3.3 Morning-evening differences

To examine the differences in the SO_2 distributions from morning and evening overpasses, we focus hereafter on a large area (30–40° N/105–117° E) above China. For this region and for each month in the period 1 January 2008–30 September 2014, we first calculate for morning and evening the fraction of successful SO_2 retrievals, i.e. those that pass the prior and posterior filters described in the previous sections and for which the HRI has a correspondence in the LUTs, relative to all the retrievals performed in the considered area. Regarding the last condition, it is important to point out that we found that a number of IASI measurements, mainly associated with negative thermal contrast, were not covered by the LUTs. The fraction of these measurements is shown in Fig. 9 (left, second panel from top), along with the fraction of successful SO_2 retrievals (top panel), as time series. They are compared (as in Fig. 8) to the time evolution of thermal contrast (third panel from top) and water content (bottom panel).

From the top panel we see that the amount of successful retrievals during the evening orbit is significantly smaller than during the morning orbit of IASI. In the morning the seasonality is marked, with successful retrievals varying from close to zero in the humid summer months to 20–60 % from January to May. For the evening measurements, the number of successful retrievals stays low year-round and is above 5 % only for one or two months in spring. The prime rejection criterion for the evening measurements is surprisingly the absence of correspondence, for given angles, thermal contrasts and humidity, between measured and simulated HRI in the LUTs, as obvious from the second panel. This is especially the case in winter (60–80 % of rejected measurements), when thermal contrast is negative and humidity low.

AMTD
8, 11029–11075, 2015

The fact that such situations are not included in the LUTs comes very likely from a misrepresentation of nighttime atmospheric temperature profiles and in particular temperature inversions with the conditions used to build the LUTs (Table 1). To illustrate this, Fig. 9 (right) shows a comparison between the standard temperature profile used and a typical profile retrieved above China (35.81°N–117.81°E) on the 29 December 2013. This is a situation for which the thermal contrast is −5 K and the water column 2.42×10^{22} molecules cm^{-2}, and for which the measured HRI value of −3.9 has no correspondence in the LUTs. The simulation of a IASI spectrum with these two temperature profiles, assuming a SO_2 column of 4.35 DU, results in totally different values of the HRI, +1.2 for the US Standard temperature profile and −4.1 for the retrieved temperature profile. These results pinpoint a limitation of the current LUTs for slightly negative thermal contrast (it is not observed for large temperature inversions), which is a range where the competition between absorption and emission contributions to the HRI vary drastically. More work will be needed to avoid this shortcoming of the method in the future, either by including more temperature profiles in the calculation of the LUTs or by using alternative approaches to better account for the variety of real situations encountered. Note that errors on the thermal contrast also affect the HRI and, as a consequence, the retrieved SO_2 column. They could be partly responsible for the observed non correspondence between measured HRI and the LUTs.

The small number of successful retrievals in the evening measurements combined with the generally lower sensitivity of IASI in this period of the day, is likely responsible in part for the factor 2–3 difference observed in the SO_2 columns between morning and evening measurements. Indeed, as only the retrieved SO_2 columns with small errors are kept and as these are in the evening mainly those with large columns, the averages are biased high. The effect probably also exists for the morning measurements but is less pronounced because of the better sensitivity to smaller columns with the atmospheric conditions – particularly thermal contrast – encountered. Another possible cause for the larger concentrations is photochemistry. During the day, the photochemistry is more active and the concentrations of oxidants such as OH, H_2O_2 and

AMTD
8, 11029–11075, 2015

O_3 are high, creating an important sink for SO_2, which disappears at night, favourising higher concentrations. Such a diurnal cycle of SO_2 has been observed previously in China (Wang, 2002; Wang et al., 2014) and in other regions of the world (Khemani et al., 1987; Psiloglou et al., 2013) but in others, noontime SO_2 peaks have also been observed (e.g. Lin et al., 2012; Xu et al., 2014), possibly as a result of other meteorological/dynamical effects (Xu et al., 2014).

3.4 Product evaluation

3.4.1 Comparisons with an optimal estimation retrieval scheme

As already mentioned in Sect. 3.1, Norilsk is an industrial area located in Siberia that emits large quantities of SO_2. Recently, taking the advantages of the large temperature inversions that develop in winter in the region, we have monitored for the first time SO_2 in this area with the IASI sounder over several years (Bauduin et al., 2014), by using a method relying on the iterative Optimal Estimation (Rodgers, 2000) and exploiting a generalized spectral noise covariance matrix (see also Carboni et al., 2012). As a first assessment of the low-altitude SO_2 column product developed in this work, we compare the resulting 0–4 km SO_2 columns with the 0–5 km columns retrieved by Bauduin et al. (2014). The results are presented in Fig. 10. For the comparison, we consider measurements located in a circle of 150 km radius around the city of Norilsk, with less than 25 % cloud fraction, with a thermal contrast larger than 5 K in absolute value and with a humidity below 4 g kg^{-1} at 350 m above ground (this altitude corresponds to the average height of the temperature inversions). These last conditions ensure that near-surface SO_2 is indeed probed, as explained in Bauduin et al. (2014) and also well seen in their Fig. 3. Finally, we only consider the SO_2 columns retrieved with the method described in this work with less than 25 % of relative error and less than 10 DU absolute error. The entire period 2008–2013 is analyzed, resulting in a total of 1233 pairs of columns to compare. The comparison between the two sets of SO_2 columns is shown in Fig. 10. A linear regression is also shown between the two coinci-

AMTD
8, 11029–11075, 2015

dent sets of data using the reduced major axis method (Smith et al., 2009) to account for the fact that both datasets come with errors. The agreement between the columns is very good, characterized by a correlation coefficient of 0.94. The intercept, which is close to zero, and the slope of 0.80 indicate that the SO_2 columns retrieved using the LUT tend to be 20 % smaller than those retrieved with the iterative method of Bauduin et al. (2014). This difference is partly due to the difference in columns (0–4 km with the newly developed method against 0–5 km in Bauduin et al.) and to the difference in the profile used to build the LUTs with the a priori profile used in the iterative method. The use of the constant temperature profile for the LUTs can also cause this difference.

Finally, it is worth to emphasize in Fig. 10 the measurements for which the LUTs provide a column above 2.5–3 DU and the optimal estimation retrieval a column close to 0 corresponding to the a priori column. As obvious from the color scale these retrievals are all associated with a relatively high humidity of 3 g kg^{-1}. These measurements have a significant HRI around 5, indicating small but sufficient signal strength, for which the iterative method has difficulties. This result shows the strength of the LUT-approach for these low-signal cases.

3.4.2 Comparisons with OMI derived SO_2 columns

OMI is an imaging spectrograph that operates in a nadir-viewing mode in the ultraviolet-visible spectral range 270–500 nm, and was launched in 2004 on the EOS-Aura NASA platform (details are given in Levelt et al., 2006). We perform a comparison of the retrieved 0–4 km SO_2 column from IASI to those retrieved from OMI using the algorithm of Theys et al. (2015) for anthropogenic SO_2. For the IASI column, the same filters on cloud fraction and errors as described in Sects. 3.1 and 3.2 are applied. For the OMI columns, only those retrieved in the spectral range 312–326 nm from measurements not too much affected by the row anomaly, with solar zenith angles smaller than 65° and less than 30 % cloud fraction are used (see Theys et al., 2015, for details). The comparison is performed on monthly averages for the period 2010–2013 and for an area corresponding to a circle of 125 km around Beijing. Figure 11 shows the com-

AMTD
8, 11029–11075, 2015

parison in terms of a time series of the monthly averaged columns of IASI (blue) and OMI (red squares for the standard retrieval and green triangles for the retrieval using a different air mass factor (AMF)). From Fig. 11, it can be seen that the IASI columns are on average a factor 2.5 larger. The mean relative difference between the monthly averages of the two instruments is −135 % (OMI-IASI/OMI). This difference has several origins. Firstly, monthly means calculated from IASI are probably overestimated by the fact that only the columns with low errors are kept, which favors the higher values of the columns. Secondly, it is likely that OMI SO_2 columns are underestimated. This has already been observed by Theys et al. (2015) above Xianghe (China), in the comparison with MAX-DOAS measurements (Wang et al., 2014) and explained by the inappropriate AMF used to convert the OMI derived SO_2 slant column densities (SCD) in vertical column densities (VCD). In their study, Theys et al. showed that the use of better AMF significantly improves the agreement between MAX-DOAS and OMI observations. For the sake of illustration, we also show in Fig. 11 the SO_2 vertical column densities from OMI retrieved using the method of Theys et al., but with a constant AMF of 0.4, which is the one used in the operational OMI PBL SO_2 product (Krotkov et al., 2008). With this correction, the agreement between the two instruments is improved; the mean relative difference becomes −65 %. Discrepancies remain but are probably within the range of what we can expect given the likely high-bias of IASI monthly averages and the difference in the overpass times of the two satellites.

4 Conclusions

In this work, we have presented a method for retrieving SO_2 in the low troposphere from IASI at a global scale. The method follows two steps, both relying on the calculation of radiance indexes (HRI), which represent the strength of SO_2 spectral signal in IASI measurements. In the first step, the altitude of SO_2 plumes is retrieved and all plumes with altitude above 4 km (from ground), likely from volcanic origin, are rejected. For the remaining low-altitude plumes, HRI values are converted into SO_2 0–4 km (ground to

AMTD
8, 11029–11075, 2015

4 km above it) columns using look-up tables. The construction of the LUTs is a key part of the method: it is done from forward model simulations taking into account the thermal contrast, the total column of H_2O and the zenith angle. Tables of errors have been associated with each LUT, allowing the error characterization of each retrieved SO_2 column and the posterior selection of the retrieved SO_2 columns for which IASI is sensitive enough.

The method has been applied to IASI data from 1 January 2008 to 30 September 2014 to provide global distributions and time series for the 0–4 km column. The average global distribution reveals the large known anthropogenic SO_2 sources, such as the Norilsk and Sar Cheshmeh smelters, the power plants in South Africa and the large industrial region in North-East China. Smaller sources, e.g. power plants in Bulgaria, are also measured. In addition to this, low altitude plumes from degassing volcanoes are also detected. Non-negligible SO_2 columns have been retrieved above the Taklamakan desert and this was explained by enhanced sensitivity of IASI in this region characterized by extremely low humidity and high thermal contrast; the source of the SO_2 remains to be assessed. Similarly, the generally favorable conditions occurring in Sar Cheshmeh (Iran) have allowed acquiring the daily time evolution of the SO_2 column almost completely over the entire 7 years. This was not the case for the Beijing area that we selected as another example region, where we show that IASI sensitivity has a strong seasonal cycle such that the SO_2 columns can only be retrieved with small errors for the period December–May, corresponding to the driest months. The retrieved SO_2 0–4 km columns from IASI have been compared to those of OMI on a monthly-averaged basis. A high-bias of 135 % has been revealed, decreasing to 65 % depending on the choice of the AMF used in the OMI retrievals. More comparisons are still required to investigate deeper these observed differences. Another assessment of the retrieval method was provided by comparing the retrieved SO_2 columns from IASI with the LUT based approach to those retrieved from the same measurements with an iterative optimal estimation scheme; a good correspondence was found between the two column datasets (correlation coefficient of 0.94, with the LUT lower by 20 %)

AMTD
8, 11029–11075, 2015

considering the different assumptions and input profiles used in the two methods. This excellent agreement shows how well the new method is able to retrieve near-surface SO_2. It has the advantage of being very fast; iterations and the retrieval of interfering parameters are not needed. It is also very sensitive and has shown interestingly better results for weak SO_2 signals.

Finally, striking differences between morning and evening SO_2 distributions retrieved from IASI were shown, with the SO_2 columns retrieved in the evening being more confined spatially and larger than those from the morning by a factor 2–3. While changes in photochemistry could explain part of this effect, we have shown that it is most probably due to a shortcoming with the LUT, which rely on a single temperature profile and are not able to deal well with temperature inversions, which develop in the evening and in winter. Further developments will be needed to correct for this and to allow a better representativeness of the variety of temperature and humidity conditions occurring globally. The use of the ν_1 band can also be envisaged to reduce the impact of humidity and increase the number of used data. Despite this, given the preliminary comparisons, the results obtained with this new method are however very encouraging, especially for daytime, and constitute the first successful attempt to retrieve near-surface SO_2 globally with the IASI thermal infrared sensor. The continuation of this program is ensured by the soon coming launch of MetOp-C (2018) and on a longer term by the IASI-NG mission onboard MetOp-SG (Crevoisier et al., 2014).

Acknowledgements. IASI has been developed and built under the responsibility of the Centre National d'Etudes Spatiales (CNES, France). It is flown on board the MetOp satellites as part of the EUMETSAT Polar System. The IASI L1 data are received through the EUMETCast near real-time data distribution service. The research in Belgium was funded by the F.R.S-FNRS, the Belgian State Federal Office for Scientific, Technical, and Cultural Affairs, and the European Space Agency (ESA-Prodex arrangements). Financial support by the "Actions de Recherche Concertée" (Communauté Française de Belgique) is also acknowledged. S. Bauduin, L. Clarisse and P.-F. Coheur are respectively Research Fellow, Research Associate and Senior Research Associate with F.R.S.-FNRS. C. Clerbaux is grateful to CNES for scientific collaboration and financial support. We would like to thank D. Hurtmans for the development

AMTD
8, 11029–11075, 2015

of the Atmosphit software. We also acknowledge the Ether/ECCAD database for the archiving and the distribution of the EDGAR v4.2 emission inventory.

References

Ali-Khodja, H. and Kebabi, B.: Assessment of wet and dry deposition of SO_2 attributable to a sulfuric acid plant at Annaba, Algeria, Environ. Int., 24, 799–807, doi:10.1016/s0160-4120(98)00059-2, 1998. 11031

Arctic Monitoring and Assessment Programme (AMAP): Acidifying Pollutants, Arctic Haze, and Acidification in the Arctic, Chap. 9, 621–659, Arctic Monitoring and Assessment Programme (AMAP), Oslo, Norway, 1998. 11042

Arctic Monitoring and Assessment Programme (AMAP): Acidifying Pollutants, Arctic Haze, and Acidification in the Arctic, Arctic Monitoring and Assessment Programme (AMAP), Oslo, Norway, 2006. 11042

Anderson, G., Clough, S., Kneizys, F., Chetwynd, J., and E. P., S.: AFGL Atmospheric Constituent Profiles (0–120 km), AFGL-TR-86-0110, Environ. Res. Papers, 954, ADA175173, 1986. 11037

Andres, R. J. and Kasgnoc, A. D.: A time-averaged inventory of subaerial volcanic sulfur emissions, J. Geophys. Res., 103, 25251–25261, doi:10.1029/98jd02091, 1998. 11031

Ardestani, M. and Shafie-Pour, M.: Environmentally compatible energy resource production-consumption pattern (case study: Iran), Environ. Devel. Sustain., 11, 277–291, doi:10.1007/s10668-007-9110-7, 2009. 11042

August, T., Klaes, D., Schlüssel, P., Hultberg, T., Crapeau, M., Arriaga, A., O'Carroll, A., Coppens, D., Munro, R., and Calbet, X.: IASI on Metop-A: Operational Level 2 retrievals after five years in orbit, J. Quant. Spectrosc. Ra., 113, 1340–1371, doi:10.1016/j.jqsrt.2012.02.028, 2012. 11035

Bauduin, S., Clarisse, L., Clerbaux, C., Hurtmans, D., and Coheur, P.-F.: IASI observations of sulfur dioxide (SO_2) in the boundary layer of Norilsk, J. Geophys. Res.-Atmos., 119, 4253–4263, doi:10.1002/2013JD021405, 2014. 11032, 11037, 11038, 11042, 11049, 11050, 11074

Blacksmith Institutes: The World's Worst Polluted Places – The Top Ten of The Dirty Thirty, The Blacksmith Institutes, New York, USA, 2007. 11042

AMTD
8, 11029–11075, 2015

Boynard, A. and Clerbaux, C., Clarisse, L., Safieddine, S., Pommier, M., Van Damme, M., Bauduin, S., Oudot, C., Hadji-Lazaro, J., Hurtmans, D., and Coheur, P.-F.: First space measurements of simultaneous pollutants in the boundary layer from IASI: a case study in the North China Plain, Geophys. Res. Lett., 41, 645–651, doi:10.1002/2013GL058333, 2014. 11032

Campion, R.: New lava lake at Nyamuragira volcano revealed by combined ASTER and OMI SO_2 measurements, Geophys. Res. Lett., 41, 7485–7492, doi:10.1002/2014gl061808, 2014. 11043

Carboni, E., Grainger, R., Walker, J., Dudhia, A., and Siddans, R.: A new scheme for sulphur dioxide retrieval from IASI measurements: application to the Eyjafjallajökull eruption of April and May 2010, Atmos. Chem. Phys. Discuss., 12, 11861–11897, doi:10.5194/acpd-12-11861-2012, 2012. 11049

Carn, S. A., Krueger, A. J., Bluth, G. J. S., Schaefer, S. J., Krotkov, N. A., Watson, I. M., and Datta, S.: Volcanic eruption detection by the Total Ozone Mapping Spectrometer (TOMS) instruments: a 22-year record of sulphur dioxide and ash emissions, Geol. Soc. Spec. Publ., 213, 177–202, doi:10.1144/gsl.sp.2003.213.01.11, 2003. 11031

Carn, S. A., Strow, L. L., De Souza-Machado, S., Edmonds, Y., Hannon, S.: Quantifying tropospheric volcanic emissions with AIRS: the 2002 eruption of Mt. Etna (Italy), Geophys. Res. Lett., 32, L02301, doi:10.1029/2004GL021034, 2005. 11031

Carn, S. A., Krueger, A. J., Krotkov, N. A., Yang, K., and Levelt, P. F.: Sulfur dioxide emissions from Peruvian copper smelters detected by the Ozone Monitoring Instrument, Geophys. Res. Lett., 34, L09801, doi:10.1029/2006GL029020, 2007. 11032, 11043

Carn, S. A., Krotkov, N. A., Yang, K., and Krueger, A. J.: Measuring global volcanic degassing with the Ozone Monitoring Instrument (OMI), Geol. Soc. Spec. Publ., 380, 229–257, doi:10.1144/sp380.12, 2013. 11043

Clarisse, L., Coheur, P. F., Prata, A. J., Hurtmans, D., Razavi, A., Phulpin, T., Hadji-Lazaro, J., and Clerbaux, C.: Tracking and quantifying volcanic SO_2 with IASI, the September 2007 eruption at Jebel at Tair, Atmos. Chem. Phys., 8, 7723–7734, doi:10.5194/acp-8-7723-2008, 2008. 11031, 11035

Clarisse, L., Shephard, M. W., Dentener, F., Hurtmans, D., Cady-Pereira, K., Karagulian, F., Van Damme, M., Clerbaux, C., and Coheur, P.-F.: Satellite monitoring of ammonia: A case study of the San Joaquin Valley, J. Geophys. Res., 115, D13302, doi:10.1029/2009JD013291, 2010. 11039

AMTD
8, 11029–11075, 2015

Clarisse, L., Coheur, P.-F., Prata, F., Hadji-Lazaro, J., Hurtmans, D., and Clerbaux, C.: A unified approach to infrared aerosol remote sensing and type specification, Atmos. Chem. Phys., 13, 2195–2221, doi:10.5194/acp-13-2195-2013, 2013. 11036

Clarisse, L., Coheur, P.-F., Theys, N., Hurtmans, D., and Clerbaux, C.: The 2011 Nabro eruption, a SO_2 plume height analysis using IASI measurements, Atmos. Chem. Phys., 14, 3095–3111, doi:10.5194/acp-14-3095-2014, 2014. 11032, 11034, 11035, 11036, 11045

Clerbaux, C., Coheur, P.-F., Clarisse, L., Hadji-Lazaro, J., Hurtmans, D., Turquety, S., Bowman, K., Worden, H., and Carn, S.: Measurments of SO_2 profiles in volcanic plumes from the NASA Tropospheric Emission Spectrometer (TES), Geophys. Res. Lett., 35, L22807, doi:10.1029/2008GL035566, 2008. 11031

Clerbaux, C., Boynard, A., Clarisse, L., George, M., Hadji-Lazaro, J., Herbin, H., Hurtmans, D., Pommier, M., Razavi, A., Turquety, S., Wespes, C., and Coheur, P.-F.: Monitoring of atmospheric composition using the thermal infrared IASI/MetOp sounder, Atmos. Chem. Phys., 9, 6041–6054, doi:10.5194/acp-9-6041-2009, 2009. 11033

Coheur, P.-F., Barret, B., Turquety, S., Hurtmans, D., Hadji-Lazaro, J., and Clerbaux, C.: Retrieval and characterization of ozone vertical profiles from a thermal infrared nadir sounder, J. Geophys. Res., 110, D24303, doi:10.1029/2005JD005845, 2005. 11037

Crevoisier, C., Clerbaux, C., Guidard, V., Phulpin, T., Armante, R., Barret, B., Camy-Peyret, C., Chaboureau, J.-P., Coheur, P.-F., Crépeau, L., Dufour, G., Labonnote, L., Lavanant, L., Hadji-Lazaro, J., Herbin, H., Jacquinet-Husson, N., Payan, S., Péquignot, E., Pierangelo, C., Sellitto, P., and Stubenrauch, C.: Towards IASI-New Generation (IASI-NG): impact of improved spectral resolution and radiometric noise on the retrieval of thermodynamic, chemistry and climate variables, Atmos. Meas. Tech., 7, 4367–4385, doi:10.5194/amt-7-4367-2014, 2014. 11053

de Foy, B., Krotkov, N. A., Bei, N., Herndon, S. C., Huey, L. G., Martínez, A.-P., Ruiz-Suárez, L. G., Wood, E. C., Zavala, M., and Molina, L. T.: Hit from both sides: tracking industrial and volcanic plumes in Mexico City with surface measurements and OMI SO_2 retrievals during the MILAGRO field campaign, Atmos. Chem. Phys., 9, 9599–9617, doi:10.5194/acp-9-9599-2009, 2009. 11043

European Commission, Joint Research Centre (JRC)/Netherlands Environmental Assessment Agency (PBL): Emission Database for Global Atmosphere Research (EDGAR), release version 4.2, available at: http://edgar.jrc.ec.europa.eu, 2011. 11041

AMTD
8, 11029–11075, 2015

Eisinger, M. and Burrows, J. P.: Tropospheric sulfur dioxide observed by the ERS-2 GOME instrument, Geophys. Res. Lett., 25, 4177–4180, 1998. 11031, 11044

Emmons, L. K., Walters, S., Hess, P. G., Lamarque, J.-F., Pfister, G. G., Fillmore, D., Granier, C., Guenther, A., Kinnison, D., Laepple, T., Orlando, J., Tie, X., Tyndall, G., Wiedinmyer, C., Baughcum, S. L., and Kloster, S.: Description and evaluation of the Model for Ozone and Related chemical Tracers, version 4 (MOZART-4), Geosci. Model Dev., 3, 43–67, doi:10.5194/gmd-3-43-2010, 2010. 11037

Fioletov, V. E., McLinden, C. A., Krotkov, N., Moran, M. D., and Yang, K.: Estimation of SO_2 emissions using OMI retrievals, Geophys. Res. Lett., 38, L21811, doi:10.1029/2011GL049402, 2011. 11032

Fioletov, V. E., McLinden, C. A., Krotkov, N., Yang, K., Loyola, D. G., Valks, P., Theys, N., Van Roozendael, M., Nowlan, C. R., Chance, K., Liu, X., Lee, C., and Martin, R. V.: Application of OMI, SCIAMACHY, and GOME-2 satellite SO_2 retrievals for detection of large emission sources, J. Geophys. Res.-Atmos., 118, 11399–11418, doi:10.1002/jgrd.50826, 2013. 11032, 11042

Fioletov, V. E., McLinden, C. A., Krotkov, N., and Li, C.: Lifetimes and emissions of SO_2 from point sources estimated from OMI, Geophys. Res. Lett., 42, 1969–1976, doi:10.1002/2015gl063148, 2015. 11032

Ganci, G., Harris, A. J. L., Del Negro, C., Guehenneux, Y., Cappello, A., Labazuy, P., Calvari, S., and Gouhier, M.: A year of lava fountaining at Etna: volumes from SEVIRI, Geophys. Res. Lett., 39, L06305, doi:10.1029/2012gl051026, 2012. 11043

Grutter, M., Basaldud, R., Rivera, C., Harig, R., Junkerman, W., Caetano, E., and Delgado-Granados, H.: SO_2 emissions from Popocatépetl volcano: emission rates and plume imaging using optical remote sensing techniques, Atmos. Chem. Phys., 8, 6655–6663, doi:10.5194/acp-8-6655-2008, 2008. 11043

Halmer, M., Schmincke, H.-U., and Graf, H.-F.: The annual volcanic gas input into the atmosphere, in particular into the stratosphere: a global data set for the past 100 years, J. Volcanol. Geoth. Res., 115, 511–528, doi:10.1016/s0377-0273(01)00318-3, 2002. 11031

Hilton, F., Armante, R., August, T., Barnet, C., Bouchard, A., Camy-Peyret, C., Capelle, V., Clarisse, L., Clerbaux, C., Coheur, P.-F., Collard, A., Crevoisier, C., Dufour, G., Edwards, D., Faijan, F., Fourrié, N., Gambacorta, A., Goldberg, M., Guidard, V., Hurtmans, D., Illingworth, S., Jacquinet-Husson, N., Kerzenmacher, T., Klaes, D., Lavanant, L., Masiello, G., Matricardi, M., McNally, A., Newman, S., Pavelin, E., Payan, S., Péquignot, E., Peyridieu, S.,

AMTD
8, 11029–11075, 2015

Phulpin, T., Remedios, J., Schlüssel, P., Serio, C., Strow, L., Stubenrauch, C., Taylor, J., Tobin, D., Wolf, W., and Zhou, D.: Hyperspectral Earth observation from IASI – Five Years of Accomplishments, B. Am. Meteorol. Soc., 93, 347–370, doi:10.1175/BAMS-D-11-00027.1, 2012. 11033

Huneeus, N., Gallardo, L., and Rutllant, J. A.: Offshore transport episodes of anthropogenic sulfur in northern Chile: potential impact on the stratocumulus cloud deck, Geophys. Res. Lett., 33, L19819, doi:10.1029/2006gl026921, 2006. 11043

Josipovic, M., Annegarn, H. J., Kneen, M. A., Pienaar, J. J., and Piketh, S. J.: Concentrations, distributions and critical level exceedance assessment of SO_2, NO_2 and O_3 in South Africa, Environ. Monit. Assess., 171, 181–196, doi:10.1007/s10661-009-1270-5, 2009. 11042

Kearney, C. S., Dean, K., Realmuto, V. J., Watson, I. M., Dehn, J., and Prata, F.: Observations of SO_2 production and transport from Bezymianny volcano, Kamchatka using the MODerate resolution Infrared Spectroradiometer (MODIS), Int. J. Remote Sensing, 29, 6647–6665, doi:10.1080/01431160802168392, 2008. 11043

Khemani, L. T., Momin, G. A., and Singh, G.: Variations in trace gas concentrations in different environments in India, Pure Appl. Geophys., 125, 167–181, doi:10.1007/bf00878620, 1987. 11049

Krotkov, N. A., Carn, S. A., Krueger, A. J., Bhartia, P. K., and Yang, K.: Band residual difference algorithm for retrieval of SO_2 from the aura Ozone Monitoring Instrument (OMI), IEEE Trans. Geosci. Remote, 44, 1259–1266, doi:10.1109/TGRS.2005.861932, 2006. 11031, 11032

Krotkov, N. A., McClure, B., Dickerson, R. R., Carn, S. A., Li, C., Bhartia, P. K., Yang, K., Krueger, A. J., Li, Z., Levelt, P. F., Chen, H., Wang, P., and Lu, D.: Validation of SO_2 retrievals from the Ozone Monitoring Instrument over NE China, J. Geophys. Res., 113, D16S40, doi:10.1029/2007JD008818, 2008. 11032, 11051

Krueger, A. J.: Sighting of El Chichon sulfur dioxide clouds with the Nimbus 7 Total Ozone Mapping Spectrometer, Science, 220, 1377–1379, doi:10.1126/science.220.4604.1377, 1983. 11031

Lee, C., Richter, A., Weber, M., and Burrows, J. P.: SO_2 Retrieval from SCIAMACHY using the Weighting Function DOAS (WFDOAS) technique: comparison with Standard DOAS retrieval, Atmos. Chem. Phys., 8, 6137–6145, doi:10.5194/acp-8-6137-2008, 2008. 11031

Lee, C., Martin, R. V., Van Donkelaar, A., Lee, H., Dickerson, R. R., Hains, J. C., Krotkov, N., Richter, A., Vinnikov, K., and Schwab, J. J.: SO_2 emissions and lifetimes: Estimates from

AMTD
8, 11029–11075, 2015

inverse modeling using in situ and global, space-based (SCIAMACHY and OMI) observations, J. Geophys. Res., 116, D06304, doi:10.1029/2010JD014758, 2011. 11031
Levelt, P., van den Oord, G., Dobber, M., Malkki, A., Visser, H., de Vries, J., Stammes, P., Lundell, J., and Saari, H.: The ozone monitoring instrument, IEEE T. Geosci. Remote, 44, 1093–1101, doi:10.1109/tgrs.2006.872333, 2006. 11050
Lin, W., Xu, X., Ma, Z., Zhao, H., Liu, X., and Wang, Y.: Characteristics and recent trends of sulfur dioxide at urban, rural, and background sites in North China: effectiveness of control measures, J. Environ. Sci., 24, 34–49, doi:10.1016/S1001-0742(11)60727-4, 2012. 11042, 11049
Lin, W., Xu, X., Yu, X., Zhang, X., and Huang, J.: Observed levels and trends of gaseous SO_2 and HNO_3 at Mt. Waliguan, China: results from 1997 to 2009, J. Environ. Sci., 25, 726–734, doi:10.1016/s1001-0742(12)60143-0, 2013. 11044
Lu, Z., Streets, D. G., Zhang, Q., Wang, S., Carmichael, G. R., Cheng, Y. F., Wei, C., Chin, M., Diehl, T., and Tan, Q.: Sulfur dioxide emissions in China and sulfur trends in East Asia since 2000, Atmos. Chem. Phys., 10, 6311–6331, doi:10.5194/acp-10-6311-2010, 2010. 11042
McLinden, C. A., Fioletov, V., Boersma, K. F., Krotkov, N., Sioris, C. E., Veefkind, J. P., and Yang, K.: Air quality over the Canadian oil sands: A first assessment using satellite observations, Geophys. Res. Lett., 39, L04804, doi:10.1029/2011GL050273, 2012. 11032
McLinden, C. A., Fioletov, V., Boersma, K. F., Kharol, S. K., Krotkov, N., Lamsal, L., Makar, P. A., Martin, R. V., Veefkind, J. P., and Yang, K.: Improved satellite retrievals of NO_2 and SO_2 over the Canadian oil sands and comparisons with surface measurements, Atmos. Chem. Phys., 14, 3637–3656, doi:10.5194/acp-14-3637-2014, 2014. 11032
Nadirov, R. K., Syzdykova, L. I., Zhussupova, A. K., and Usserbaev, M. T.: Recovery of value metals from copper smelter slag by ammonium chloride treatment, Int. J. Miner. Process., 124, 145–149, doi:10.1016/j.minpro.2013.07.009, 2013. 11042
Pougatchev, N., August, T., Calbet, X., Hultberg, T., Oduleye, O., Schlüssel, P., Stiller, B., Germain, K. St., and Bingham, G.: IASI temperature and water vapor retrievals – error assessment and validation, Atmos. Chem. Phys., 9, 6453–6458, doi:10.5194/acp-9-6453-2009, 2009. 11040
Prodanova, M., Perez, J. L., Syrakov, D., San Jose, R., Ganev, K., Miloshev, N., and Roglev, S.: Application of mathematical models to simulate an extreme air pollution episode in the Bulgarian city of Stara Zagora, Appl. Math. Modell., 32, 1607–1619, doi:10.1016/j.apm.2007.05.002, 2008. 11044

AMTD
8, 11029–11075, 2015

Psiloglou, A. E., Larissi, I. K., Petrakis, I., Paliatsos, A. G., Antoniou, N., and Viras, L. G.: Case studies on summertime measurements of O_3, NO_2, and SO_2 with a DOAS system in an urban semi-industrial region in Athens, Greece, Environ. Monit. Assess., 185, 7763–7774, doi:10.1007/s10661-013-3134-2, 2013. 11049

Rastmanesh, F., Moore, F., Kharrati-Kopaei, M., and Behrouz, M.: Monitoring deterioration of vegetation cover in the vicinity of smelting industry, using statistical methods and TM and ETM+ imageries, Sarcheshmeh copper complex, Central Iran, Environ. Monit. Assess., 163, 397–410, doi:10.1007/s10661-009-0843-7, 2010. 11042

Rastmanesh, F., Moore, F., Kharrati Kopaei, M., Keshavarzi, B., and Behrouz, M.: Heavy metal enrichment of soil in Sarcheshmeh copper complex, Kerman, Iran, Environ. Earth Sci., 62, 329–336, doi:10.1007/s12665-010-0526-2, 2011. 11042

Realmuto, V. J. and Watson, I. M.: Advances in thermal infrared mapping of volcanic sulfur dioxide, EOS Trans. AGU, 82, V32F-09, 2001. 11031

Rix, M., Valks, P., Hao, N., van Geffen, J., Clerbaux, C., Clarisse, L., Coheur, P.-F., Loyola, R., D. G., Erbertseder, T., Zimmer, W., and Emmadi, S.: Satellite monitoring of volcanic sulfur dioxide emissions for early warning of volcanic hazards, IEEE J. Sel. Top. Appl., 2, 196–206, doi:10.1109/jstars.2009.2031120, 2009. 11031

Rodgers, C. D.: Inverse Methods for Atmospheric Sounding: Theory and Practice, World Scientific, Singapore, 2000. 11049

Say, N. P.: Lignite-fired thermal power plants and SO_2 pollution in Turkey, Energy Policy, 34, 2690–2701, doi:10.1016/j.enpol.2005.03.006, 2006. 11044

Schlüssel, P., Hultberg, T. H., Phillips, P. L., August, T., and Calbet, X.: The operational IASI Level 2 processor, Adv. Space Res., 36, 982–988, doi:10.1016/j.asr.2005.03.008, 2005. 11035

Schmidt, A., Leadbetter, S., Theys, N., Carboni, E., Witham, C. S., Stevenson, J. A., Birch, C. E., Thordarson, T., Turnock, S., Barsotti, S., Delaney, L., Feng, W., Grainger, R. G., Hort, M. C., Höskuldsson, Á., Ialongo, I., Ilyinskaya, E., Jóhannsson, T., Kenny, P., Mather, T. A. Richards and Shepherd, J.: Satellite detection, long-range transport and air quality impacts of volcanic sulfur dioxide from the 2014–2015 flood lava eruption at Bardarbunga (Iceland), J. Geophys. Res.-Atmos., 120, 9739–9757, doi:10.1002/2015JD023638, 2015. 11045

Smith, R. J.: Use and misuse of the reduced major axis for line-fitting, Am. J. Phys. Anthropol., 140, 476–486, doi:10.1002/ajpa.21090, 2009. 11050

AMTD
8, 11029–11075, 2015

Smith, S. J., van Aardenne, J., Klimont, Z., Andres, R. J., Volke, A., and Delgado Arias, S.: Anthropogenic sulfur dioxide emissions: 1850–2005, Atmos. Chem. Phys., 11, 1101–1116, doi:10.5194/acp-11-1101-2011, 2011. 11031, 11042

Stebel, K., Amigo, A., Thomas, H., and Prata, A.: First estimates of fumarolic SO_2 fluxes from Putana volcano, Chile, using an ultraviolet imaging camera, J. Volcanol. Geoth. Res., 300, 112–120, doi:10.1016/j.jvolgeores.2014.12.021, 2015. 11043

Stevenson, D. S., Johnson, C. E., Collins, W. J., and Derwent, R. G.: The tropospheric sulphur cycle and the role of volcanic SO_2, Geol. Soc. Spec. Publ., 213, 295–305, doi:10.1144/GSL.SP.2003.213.01.18, 2003. 11031

Tamburello, G., Aiuppa, A., McGonigle, A. J. S., Allard, P., Cannata, A., Giudice, G., Kantzas, E. P., and Pering, T. D.: Periodic volcanic degassing behavior: the Mount Etna example, Geophys. Res. Lett., 40, 4818–4822, doi:10.1002/grl.50924, 2013. 11043

Tassi, F., Aguilera, F., Vaselli, O., Darrah, T., and Medina, E.: Gas discharges from four remote volcanoes in northern Chile (Putana, Olca, Irruputuncu and Alitar): a geochemical survey, Ann. Geophys., 54, 121–136, doi:10.4401/ag-5173, 2011. 11043

Theys, N., De Smedt, I., van Gent, J., Danckaert, T., Wang, T., Hendrick, F., Stavrakou, T., Bauduin, S., Clarisse, L., Li, C., Krotkov, N., Yu, H., Brenot, H., and Van Roozendael, M.: Sulfur dioxide vertical column DOAS retrievals from the Ozone Monitoring Instrument: global observations and comparison to ground-based and satellite data, J. Geophys. Res.-Atmos., 120, 2470–2491, doi:10.1002/2014jd022657, 2015. 11032, 11045, 11050, 11051

Van Damme, M., Clarisse, L., Heald, C. L., Hurtmans, D., Ngadi, Y., Clerbaux, C., Dolman, A. J., Erisman, J. W., and Coheur, P. F.: Global distributions, time series and error characterization of atmospheric ammonia (NH_3) from IASI satellite observations, Atmos. Chem. Phys., 14, 2905–2922, doi:10.5194/acp-14-2905-2014, 2014. 11032, 11033, 11036

Vardar, N. and Yumurtaci, Z.: Emissions estimation for lignite-fired power plants in Turkey, Energy Policy, 38, 243–252, doi:10.1016/j.enpol.2009.09.011, 2010. 11044

Varley, N. R. and Taran, Y.: Degassing processes of Popocatepetl and Volcan de Colima, Mexico, Geol. Soc. Spec. Publ., 213, 263–280, doi:10.1144/gsl.sp.2003.213.01.16, 2003. 11043

Walker, J. C., Dudhia, A., and Carboni, E.: An effective method for the detection of trace species demonstrated using the MetOp Infrared Atmospheric Sounding Interferometer, Atmos. Meas. Tech., 4, 1567–1580, doi:10.5194/amt-4-1567-2011, 2011. 11033

AMTD
8, 11029–11075, 2015

Wang, T.: Emission characteristics of CO, NO_x, SO_2 and indications of biomass burning observed at a rural site in eastern China, J. Geophys. Res., 107, ACH 9-1–ACH 9-10, doi:10.1029/2001jd000724, 2002. 11049

Wang, T., Hendrick, F., Wang, P., Tang, G., Clémer, K., Yu, H., Fayt, C., Hermans, C., Gielen, C., Müller, J.-F., Pinardi, G., Theys, N., Brenot, H., and Van Roozendael, M.: Evaluation of tropospheric SO_2 retrieved from MAX-DOAS measurements in Xianghe, China, Atmos. Chem. Phys., 14, 11149–11164, doi:10.5194/acp-14-11149-2014, 2014. 11049, 11051

Watson, I., Realmuto, V., Rose, W., Prata, A., Bluth, G., Gu, Y., Bader, C., and Yu, T.: Thermal infrared remote sensing of volcanic emissions using the moderate resolution imaging spectroradiometer, J. Volcanol. Geoth. Res., 135, 75–89, doi:10.1016/j.jvolgeores.2003.12.017, 2004. 11031

Wesely, M. L.: Parameterization of surface resistances to gaseous dry deposition in regional-scale numerical models, Atmos. Environ., 41, S52–S63, doi:10.1016/j.atmosenv.2007.10.058, 2007. 11031

Xu, W. Y., Zhao, C. S., Ran, L., Lin, W. L., Yan, P., and Xu, X. B.: SO_2 noontime-peak phenomenon in the North China Plain, Atmos. Chem. Phys., 14, 7757–7768, doi:10.5194/acp-14-7757-2014, 2014. 11049

Zhou, D. K., Larar, A. M., and Liu, X.: MetOp-A/IASI observed continental thermal IR emissivity variations, IEEE J. Sel. Top. Appl., 6, 1156–1162, doi:10.1109/JSTARS.2013.2238892, 2013. 11038

AMTD
8, 11029–11075, 2015

Table 1. Range of atmospheric situations considered for the forward model runs used as reference for the LUTs.

	Reference profile[a]	Range of values[c]
SO_2	MOZART average for polluted conditions up to 4 km; 0 above	Multiplicative factor applied on the entire reference profile: 0, 1, 5, 10, 15, 20, 30, 40, 50, 80, 100, 160, 240, 320, 640 and 1000
H_2O	US Standard	Multiplicative factor applied on the entire reference profile: 0.002, 0.005, 0.01, 0.05, 0.1, 0.2, 0.5, 1, 1.5, 1.8, 2, 2.5, 3, 3.5, 4 and 5
Thermal contrast[b]	Temperature profile from US Standard model	−30, −25, −20, −17, −15, −12, −10, −7, −5, −3, 0, 3, 5, 7, 10, 12, 15, 17, 20, 22, 25, 27, 30, 35, 40

[a] The reference profiles for SO_2, H_2O and temperature are shown in Fig. 1.
[b] Thermal contrast defined as the difference between the surface temperature (variable) and the temperature of the air at 500 m (from the reference profile).
[c] In degrees for the thermal contrast; unit less for SO_2 and H_2O scaling factors.

AMTD
8, 11029–11075, 2015

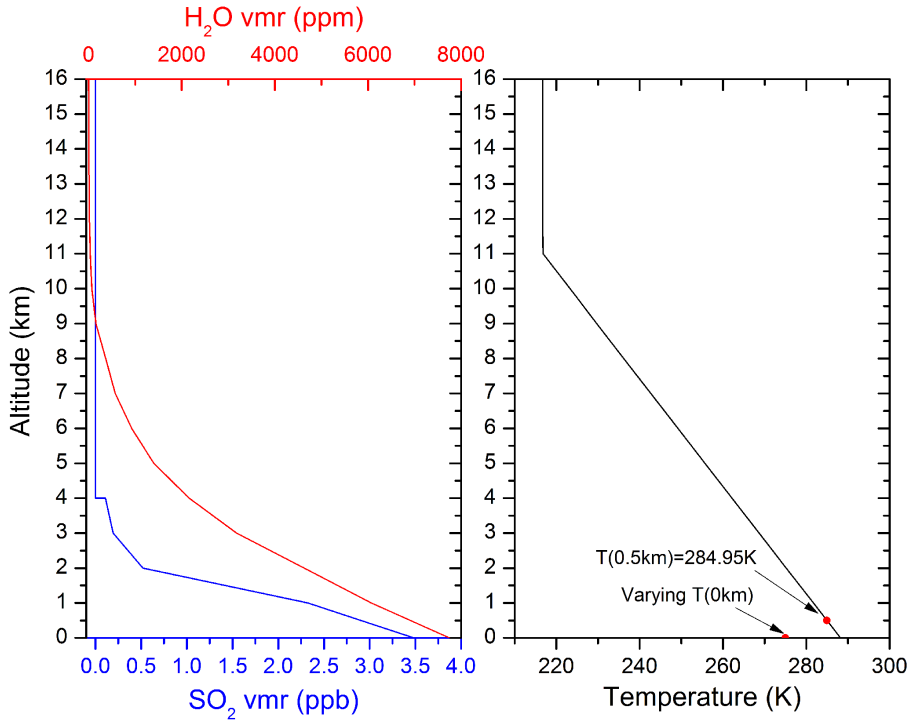

Figure 1. 2 year average SO_2 vertical profile (ppb, blue) calculated from MOZART simulations (2009–2010), US Standard water vapor profile (ppm, red) and temperature (K, right). The thermal contrast is defined as the difference between the surface temperature and the temperature of the air at 500 m (red dots).

AMTD
8, 11029–11075, 2015

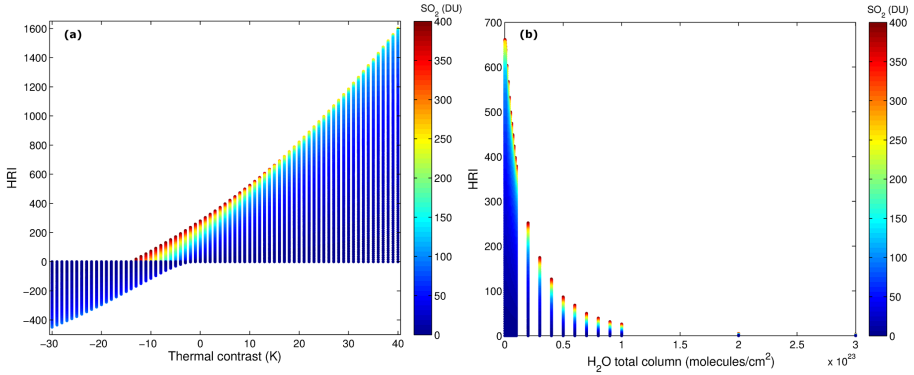

Figure 2. Example of interpolated LUT to convert HRI in SO_2 column depending on thermal contrast and water vapor for the angle bin 15–20°. The colorbar represents the 0–4 km column of SO_2 in DU. **(a)** shows the dependency of HRI on thermal contrast (constant total column of H_2O of 2×10^{20} molecules cm^{-2}); **(b)** shows the dependency on the total column of water (constant thermal contrast of 15 K).

AMTD
8, 11029–11075, 2015

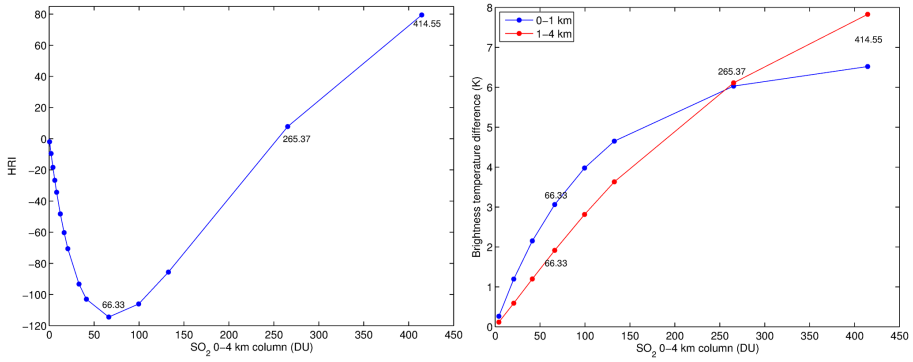

Figure 3. (left) Evolution of the HRI as function of the 0–4 km column of SO_2, in case of negative thermal contrast (−10 K). In this simulation, the total column of H_2O is of 2.4×10^{20} molecules cm^{-2} and the angle bin is 15–20°. (right) Contributions of the emission in the 0–1 km layer (blue) and of absorption in the 1–4 km layer (red) to the IASI spectrum at 1355 cm^{-1}, expressed in brightness temperature difference (absolute value). Details are given in the text.

AMTD
8, 11029–11075, 2015

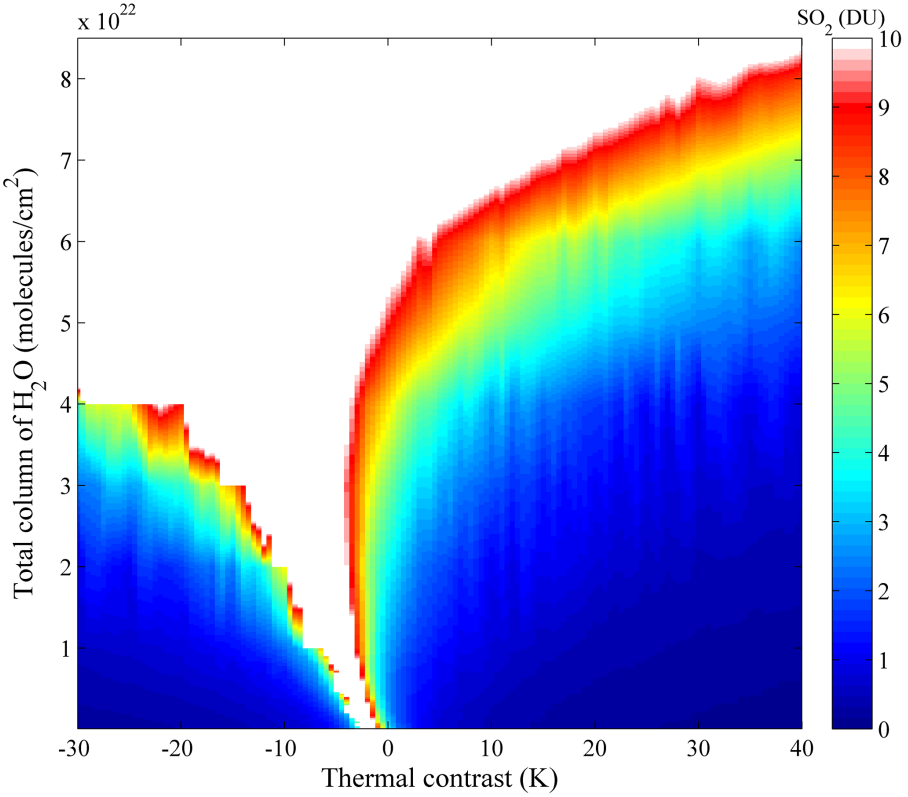

Figure 4. Lowest detectable 0–4 km SO_2 column (colorbar, in DU) as function of the thermal contrast and the total column of H_2O for the angle bin 15–20°. These columns correspond to a HRI of 3 (3σ), which can be considered as the detection threshold.

AMTD
8, 11029–11075, 2015

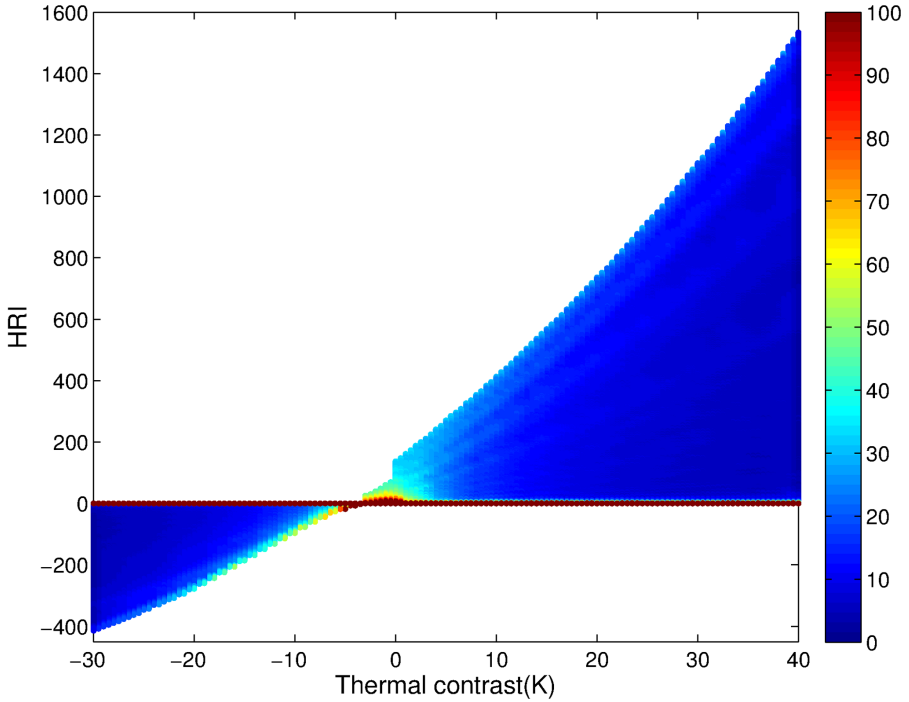

Figure 5. Relative errors (%, colorbar) as function of HRI and thermal contrast for a total column of water vapor of 2×10^{20} molecules cm^{-2} and for angle bin 0–5°.

AMTD
8, 11029–11075, 2015

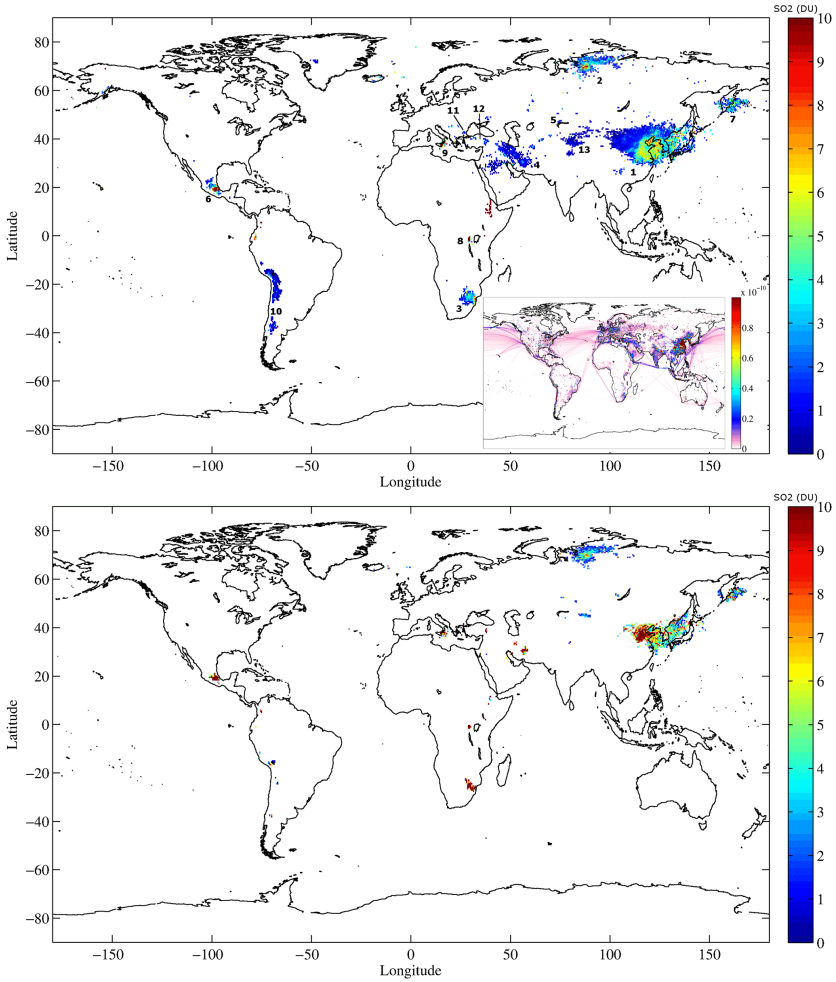

AMTD
8, 11029–11075, 2015

Global SO_2 satellite observations

S. Bauduin et al.

Figure 6. Averaged global distribution of near-surface SO_2 columns for the period 1 January 2008–30 September 2014. The top panel corresponds to daytime measurements and the bottom panel corresponds to nighttime measurements. Bottom-right inset in the daytime map represents the global anthropogenic emissions ($kg\,s^{-1}\,m^{-2}$) of SO_2 provided by the EDGARv4.2 inventory. Different sources are numbered and discussed in the text.

AMTD
8, 11029–11075, 2015

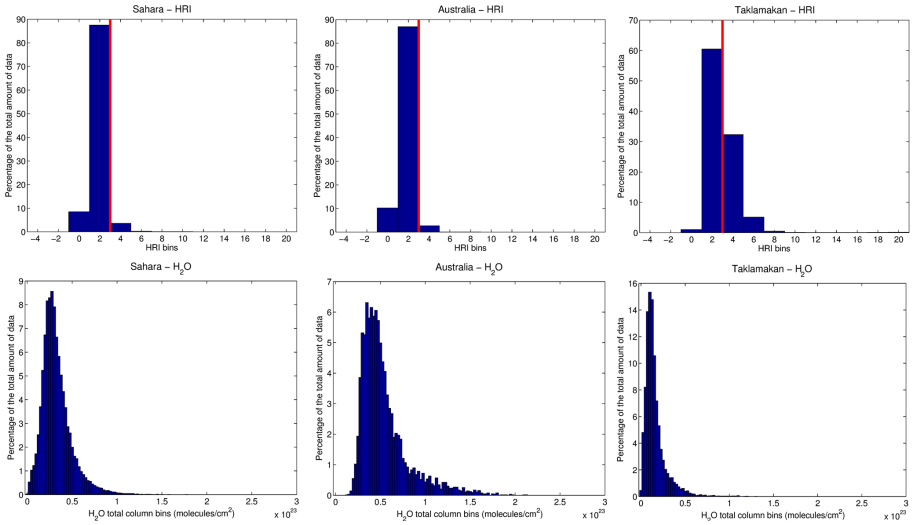

Figure 7. Distributions of IASI measurements (expressed in % of the total amount of data considered) as function of HRI values (top panels) and the total column of H_2O (bottom panels) over Sahara (left panels), center of Australia (middle panels) and Taklamakan (right panels). IASI observations for the period 2011–2014 and located in the areas 18–27° N/6° O–28° E, 29–21° S/121–140° E and 36–40° N/78–86° E have been respectively considered for Sahara, center of Australia and Taklamakan. Only those with less than 20 % of cloud coverage and with available L2 temperature and H_2O profiles and surface temperature have been selected. No filter using the error on the retrieved SO_2 column has been applied. The red lines in the top panels indicate the detection limit (see Sect. 2.3.2).

AMTD
8, 11029–11075, 2015

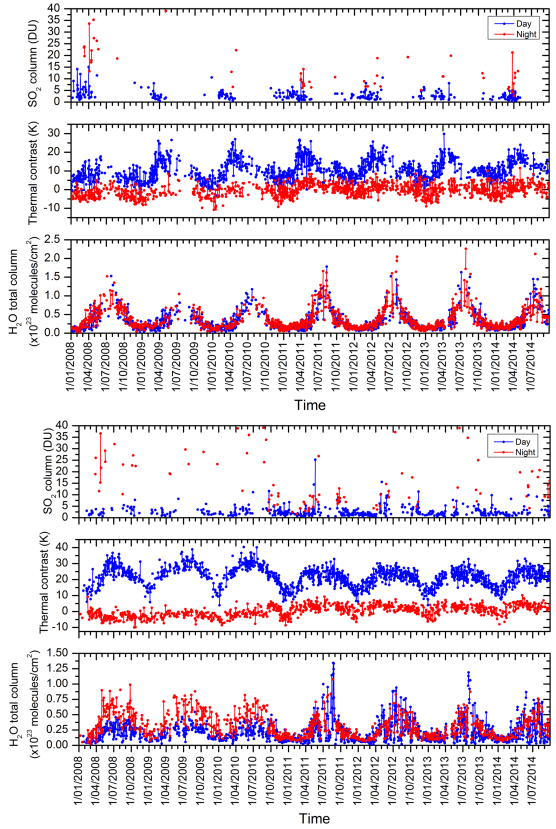

Figure 8. Daily averages of near-surface SO_2 (DU), thermal contrast (K) and H_2O total column (molecules cm^{-2}) above Beijing (top) and Sar Cheshmeh (bottom). Averages have been calculated in a circle of 125 and 75 km radius respectively for Beijing and Sar Cheshmeh. Daytime measurements are indicated in blue and nighttime measurements are indicated in red.

AMTD
8, 11029–11075, 2015

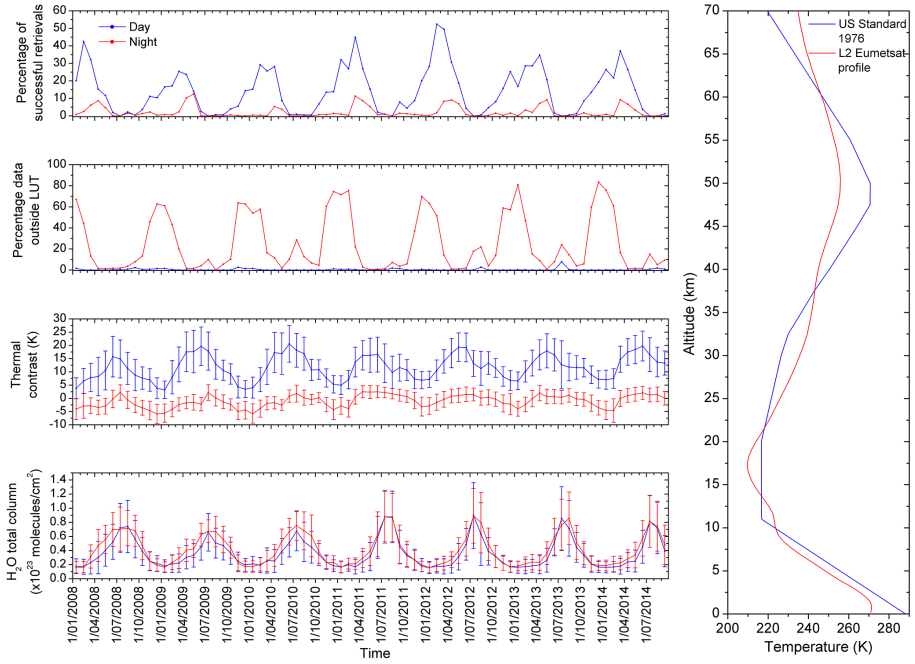

Figure 9. (left) From top to bottom (1) monthly percentage of successful retrievals (see text), (2) monthly percentage of measurements outside the LUT, (3) monthly averages of thermal contrast (K) with associated standard deviations, (4) monthly averages of the total column of H_2O (molecules cm^{-2}) with associated standard deviations. Daytime measurements correspond to blue and nighttime measurements to red. (right) Temperature vertical profiles of the US Standard 1976 model (blue) and given by the EUMETSAT L2 product (red) for the IASI spectrum recorded above China at 35.81° N–117.81° E on the 29 December 2013.

AMTD
8, 11029–11075, 2015

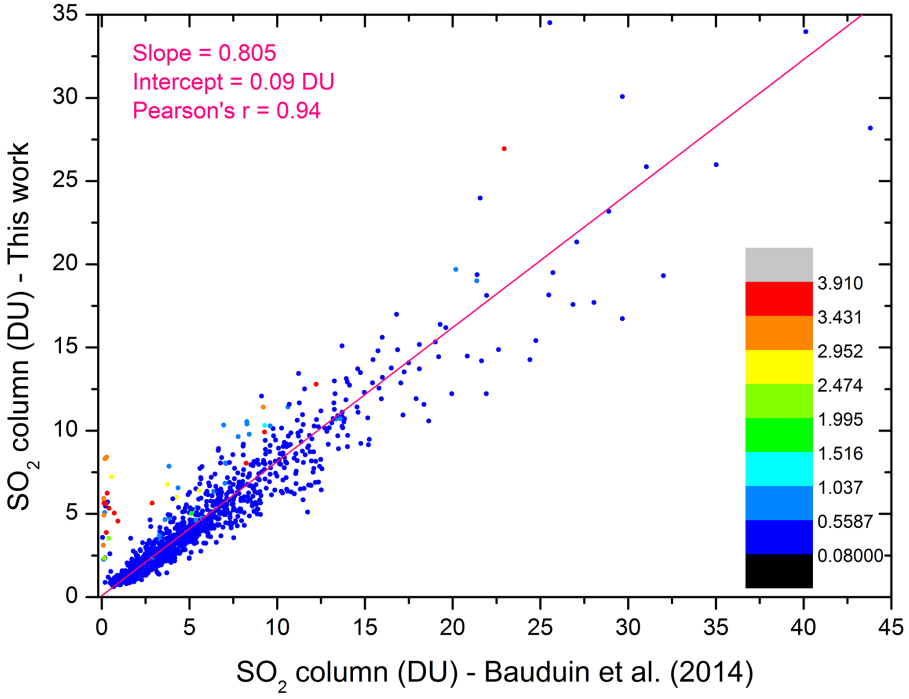

Figure 10. Comparison between SO_2 columns retrieved above the industrial area of Norilsk using the retrieval method developed in this work and the 0–5 km SO_2 columns retrieved in Bauduin et al. (2014). Measurements located in a circle of 150 km radius centered in Norilsk with less than 25 % of cloud coverage and retrieved with relative errors smaller than 25 % and absolute errors smaller than 10 DU have been taken into account. Furthermore, only measurements with H_2O amount at 350 m lower than 4 g kg^{-1} and with thermal contrast larger than 5 K in absolute value have been considered (see detailed explanations in the text). The pink line corresponds to the linear regression (reduced major axis) calculated between the two sets of data. The colorbar represents the humidity at 350 m expressed in g kg^{-1}.

AMTD
8, 11029–11075, 2015

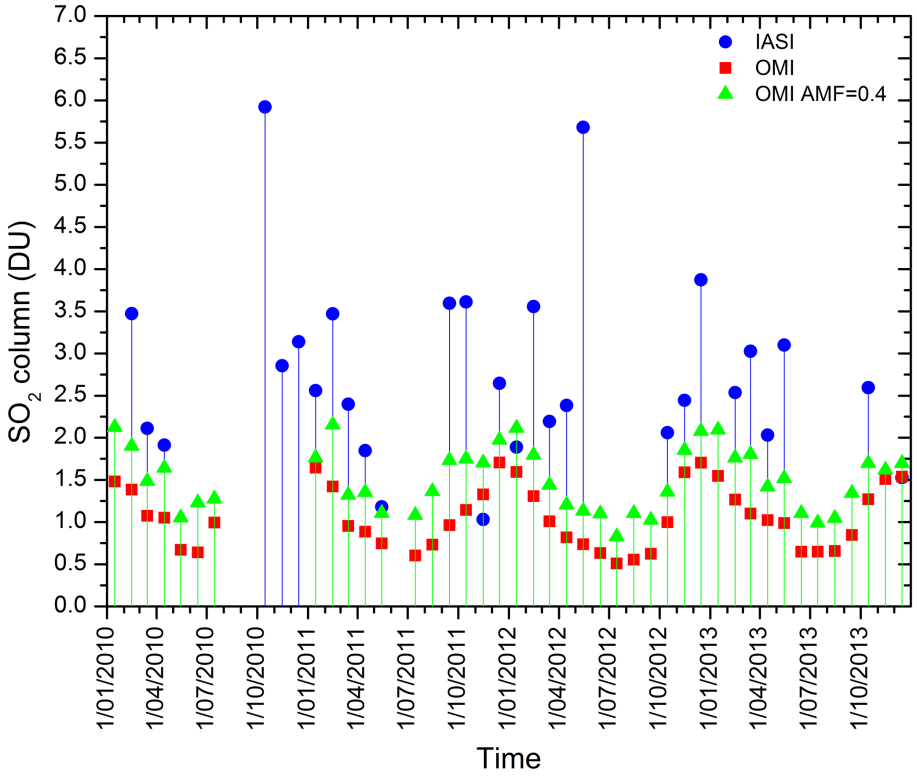

Figure 11. Monthly mean SO_2 columns (DU) retrieved for the period 2010–2013 above Beijing in a circle of 125 km radius from IASI (blue) and OMI (red) observations. Green triangles correspond to OMI measurements for which an AMF of 0.4 has been used to calculate vertical SO_2 columns. Details are given in the text.

AMTD
8, 11029–11075, 2015